Bereziskii-Kosterlitz-Thouless transition in the Weyl system PtBi2

Arthur Veyrat, Valentin Labracherie, Dima Bashlakov, Federico Caglieris, Jorge Facio, Grigory Shipunov, Titouan Charvin, Rohith Acharya, Yurii Naidyuk, Romain Giraud, et al.

To cite this version:

Arthur Veyrat, Valentin Labracherie, Dima Bashlakov, Federico Caglieris, Jorge Facio, et al.. Bereziskii-Kosterlitz-Thouless transition in the Weyl system PtBi2. Nano Letters, 2023, 23 (4), pp.1229-1235. 10.1021/acs.nanolett.2c04297 . hal-03406707

HAL Id: hal-03406707
https://hal.univ-grenoble-alpes.fr/hal-03406707v1

Submitted on 29 Nov 2021

Bereziskii-Kosterlitz-Thouless transition in the Weyl system $PtBi_2$

Arthur Veyrat [1] , Valentin Labracherie [1] , Rohith Acharya [1] , Dima L. Bashlakov[2], Federico Caglieris[1,3], Jorge I. Facio[1], Grigory Shipunov[1], Lukas Graf[1], Johannes Schoop[1,4], Yurii Naidyuk[2], Romain Giraud[1,5], Jeroen van den Brink[1,4], Bernd Büchner[1,4], Christian Hess[1,6,7], Saicharan Aswartham[1] & Joseph Dufouleur [1,6*†]

[1] *Leibniz Institute for Solid State and Materials Research (IFW Dresden), Helmholtzstraße 20, D-01069 Dresden, Germany*

[2] *B. Verkin Institute for Low Temperature Physics and Engineering, NASU, 47 Nauky Ave., 61103 Kharkiv, Ukraine*

[3] *CNR-SPIN, Corso Perrone 24, 16152 Genova, Italy*

[4] *Department of Physics, TU Dresden, D-01062 Dresden, Germany*

[5] *Université Grenoble Alpes, CNRS, CEA, Grenoble-INP, Spintec, F-38000 Grenoble, France*

[6] *Center for Transport and Devices, TU Dresden, D-01069 Dresden, Germany*

[7] *Fakultät für Mathematik und Naturwissenschaften, Bergische Universität Wuppertal, D-42097 Wuppertal, Germany*

Symmetry breaking in topological matter became, in the last decade, a key concept in condensed matter physics to unveil novel electronic states. In this work, we reveal that broken inversion symmetry and strong spin-orbit coupling in trigonal $PtBi_2$ lead to a Weyl

---

[*] Corresponding author.

[†] E-mail: j.dufouleur@ifw-dresden.de

semimetal band structure, with unusually robust two-dimensional superconductivity in thin fims. Transport measurements show that high-quality $\mathbf{PtBi_2}$ crystals are three-dimensional superconductors (T_c $\simeq$600 mK) with an isotropic critical field (B_c $\simeq$50 mT). Remarkably, we evidence in a rather thick flake (60 nm), exfoliated from a macroscopic crystal, the two-dimensional nature of the superconducting state, with a critical temperature $T_\mathrm{c} \simeq 370$ mK and highly-anisotropic critical fields. Our results reveal a Berezinskii-Kosterlitz-Thouless transition with $T_\mathrm{BKT} \simeq 310$ mK and with a broadening of Tc due to inhomogenities in the sample. Due to the very long superconducting coherence length ξ in $\mathbf{PtBi_2}$, the vortex-antivortex pairing mechanism can be studied in unusually-thick samples (at least five times thicker than for any other two-dimensional superconductor), making $\mathbf{PtBi_2}$ an ideal platform to study low dimensional superconductivity in a topological semimetal.

Keywords: Weyl semimetals, superconductivity, low dimensionality, Berezinskii-Kosterlitz-Thouless

1 Introduction

Two-dimensional (2D) superconductivity has attracted a lot of attention for more than eighty years since the discovery of the superconducting properties of Pb and Sn thin films[1]. In two dimensions, low energy fluctuations prevent the spontaneous breaking of continuous symmetries at any finite temperature[2–6]. Nevertheless, a quasi-long range correlation of an order parameter can develop at low temperature. Such an ordered phase remains very fragile and can be easily destroyed by the presence of topological point defects like vortices. The transition between the quasi-long range ordered phase and the disordered phase is called the Bereziskii-Kosterliztz-Thouless (BKT) transition[7–9]. Below the critical temperature T_{BKT}, pairing between vortex and antivortex allows a quasi-long range order. At higher temperature, the larger entropy of unbound topological defects prevails and the dissociation of vortex-antivortex pairs leads to a disordered phase[10]. Such a transition should take place in a 2D superconductor, *i.e.* when the superconducting phase coherence length ξ becomes larger than the thickness d of the superconducting film ($\xi > d$)[11,12].

The experimental evidence of a BKT transition remains generally very challenging due to the sensitivity of the ordered phase to any structural disorder[13,14]. Nevertheless, BKT transitions in 2D superconductors have been identified in different samples such as in low disordered evaporated thin films[15,16] or thin films grown by molecular beam epitaxy[17–22], exfoliated superconductors[23–27], oxide heterostructures[28], field effect transistors[29,30] and more recently in encapsulated structures based on one or several exfoliated monolayers of van der Waals materials, which are not superconducting in their bulk form[31–34]. 2D superconductivity and BKT transitions are of particular interest when they take place in materials with brocken inversion symmetry ($\mathcal{I}$) and strong spin-orbit coupling, where the electron spin degeneracy of Bloch states is lifted. This may lead to unconventional superconducting states, such as a mixed singlet and triplet superconductivity[35–37], or a Fulde-Ferrell-Larkin-Ovchinnikov (FFLO) finite momentum pairing[38–43]. It can also enable the realization of a Weyl semimetal phase, which, coupled to superconductivity, constitutes an ideal platform to study unconventional superconducting states or topological superconductivity[44–51].

In this context, $\mathrm{PtBi_2}$ is of particular interest. Beyond its very large magnetoresistance measured in the hexagonal[52] and pyrite[53] crystal structures, the spin-orbit coupling together with the broken $\mathcal{I}$ are responsible for a variety of interesting electronic properties including a strong Rashba-like spin splitting[54], triply degenerated points[55], sixfold fermion near the Fermi level[56] and non-trivial topology in the monolayer limit[57]. In this work, in addition to the unveiling of Weyl points at 48 meV above the Fermi energy, we characterize the superconducting transition of a macrosopic crystal of trigonal $PtBi_2$, from which we infer a long coherence length of 55 nm. Remarkably, we show that the superconductivity persists in a 60 nm thin exfoliated sample in which its 2D nature is evidenced and for which a Berezinsky-Kosterlitz-Thouless (BKT) transition takes place. To our knowledge, and excluding the case of effective 2D layered superconductors [58,59], the flake is five times thicker than any superconducting films exhibiting a BKT transition reported so far[60], making $PtBi_2$ a prime candidate to study low dimensional superconductivity. Among the few Weyl semimetals showing a superconducting transition under ambiant pressure[61–65], $PtBi_2$ is, together with $MoTe_2$[66], the only one exhibiting such a 2D superconductivity.

2 Results

Band structure. We studied the electronic structure of trigonal $PtBi_2$ in the space group P31m (Figure 1.a) based on the crystal structure reported in Ref. 67 and focused on the consequences of broken $\mathcal{I}$. We performed fully-relativistic density-functional calculations treating the spin-orbit coupling in the four component formalism, as implemented in Ref. 68. The energy bands along the path indicated in Figure 1.b is presented in Figure 1.c. Similar to previous works[55,67], the bandstructure indicates a semimetallic character with several bands crossing the Fermi energy, generating various electron and hole pockets. Broken $\mathcal{I}$ opens up the possibility of accidental crossing of bands at isolated points (Weyl nodes). A search for Weyl nodes between bands N and $N+1$, where N is the number of valence electrons per unit cell, yields the existence of twelve Weyl nodes, lying 48 meV above the Fermi energy. Six of the nodes are related by combinations of the three-fold rotation and reflection symmetries, while the remaining six nodes are connected to the former by time-reversal symmetry (Figure 1 b).

Usually, Weyl nodes in the bulk electronic structure induce open Fermi arcs in the surface electronic structure. A calculation based on a semi-infinite slab along the 0001 direction shows that the surface Fermi energy contours in $PtBi_2$ present a strong sensitivity to the surface termination (see SI-1). In particular, while the Weyl nodes place within the projection of the bulk Fermi surface, clear spectral weight connecting opposite chirality Weyl nodes can be observed, which is more intense for a Bi_2-terminated surface.

Magnetoresistance. To investigate the properties of $PtBi_2$, high quality single crystals of trigonal $PtBi_2$ were grown via self-flux method as described in details in Ref. 67. We first contacted bulk single crystals of $PtBi_2$ in a four probe configuration using silver wires and epoxy. A crystal was mounted on a piezo driven rotator and measured under magnetic field down to liquid helium temperature. When cooled down, the resistance decreases such that the residual resistance ratio reaches about 130 (see SI-2). At low temperature, we measured the magnetoresistance for different angles of the magnetic field ranging between -30° and 120°with 0° corresponding to an out-of-plane field and 90° to an in-plane field.

A strong anisotropy of the magnetoresistance is measured when tilting the magnetic field with respect to the orthogonal orientation and a maximum is reached for a tilt angle $\theta \sim \pm 20°$. Close to these angles, the magnetoresistance reaches 3000% at $B = 15$ T (Figure 1.d and 1.e), one order of magnitude smaller than the magnetoresistance reported in Ref. 55, but larger than what is reported in Ref. 69. For such angles, the magetoresistance is almost linear and large Shubnikov-de Haas oscillations appear at low temperature. They rapidly disappear when the angle deviates from optimized values, as reported for stoichiometric $PtBi_2$55.

Figure 1.f shows the fast Fourier transform (FFT) of the oscillations measured at 2.5 K. A single sharp peak emerges at a magnetic frequency of 345 T, in very good agreement with the main peak measured in Ref. 55. These oscillations are therefore attributed to a single pocket, the cross section of which is 3.3 nm^{-2} large, in the direction perpendicular to the magnetic field ($\theta = 20$ °). This corresponds to a typical wave vector $k \sim 1.03$ nm^{-1}.

Bulk superconductivity. When cooled down to very low temperature in a dilution fridge, the resistance decreases down to $T \sim 15$ K and remains nearly constant down to the superconducting transition at a critical temperature $T_\mathrm{c} \sim 600$ mK (see Figure 2.a and methods for the definition of the critical temperature, current and field). At $T = 100$ mK, the zero-resistance state is destroyed by the application of a 60 mT large in-plane magnetic field, corresponding to the low temperature in-plane critical field. In macroscopic structures, the critical field is found to be almost isotropic (see SI-3). Point contact measurements (see Methods) indicate that T_c increases likely due to local pressure similar to $MoTe_2$ (see inset of Figure 2.a and SI-4): the differential resistance (dV/dI)

of bulk samples shows a zero-bias drop of almost 50% at 1.55 K, at about $2.5 \times T_{\mathrm{c}}$. The drop, is still visible at temperatures up to 2.9 K, corresponding to an almost fourfold increase from zero-pressure measurements.

To further characterize the superconducting state, we measured the temperature dependency of the critical field B_{c}. In the absence of any confinement, the Ginzburg-Landau theory in three dimensions (3D) predicts a linear temperature dependence of B_{c} for T close to T_{c},

$$B_c(T) = \frac{\Phi_0}{2\pi\xi^2}\Big(1 - \frac{T}{T_c}\Big), \tag{1}$$

with $\Phi_0 = h/2e$ the superconducting flux quantum (h is the Planck constant and e the electronic charge) and ξ the superconducting coherence length at $T = 0$. The result is plotted in Figure 2.b where a linear dependence of the in-plane critical field with temperature is measured over a wide range of temperature below T_{c}. A linear fit in the temperature range allowed us to extract a large coherence length in $\mathrm{PtBi_2}$, with $\xi = 56$ nm.

Two-dimensional superconductivity. The long ξ measured in a macroscopic crystal and the 2D van der Waals layered nature of $\mathrm{PtBi_2}$ open the way to a mechanical exfoliation down to thicknesses lower than ξ in order to observe a transition from 3D to 2D superconductivity. To this end, a 57 nm thick and few tens of micron large exfoliated flake was contacted and measured down to 100mK (see Methods).

Like the bulk samples, it exhibits a superconducting transition, with a drop in the resistance to zero at $T_c = 370$ mK, almost a factor two lower than the critical temperature of the parent macroscopic crystal. To further characterize the superconducting state, we measured the differential resistance (dV/dI) as a function of a DC-current and for different temperatures below and above T_{c} (Figure 4.a and SI-6). For $T \gg T_{\mathrm{c}}$, dV/dI remains constant and equal to the equilibrium normal state resistance R_{N}. For $T \lesssim T_{\mathrm{c}}$, the superconducting transition takes place and a gap opens up leading to a vanishing dV/dI at zero bias. At high DC currents, dV/dI recovers its value of the normal state R_{N}. The transition occurs at a critical current $I_{\mathrm{c}} \sim 22\ \mu$A. The value of I_{c} is almost temperature independent well below the critical temperature and it slowly vanishes when the temperature approches T_{c} (see Figure 3.a and SI-8). The critical current depends linearly on the magnetic field for both an in-plane and an out-of plane magnetic field (see SI-7).

The critical field B_{c} is found to be strongly reduced for a perpendicular field (along the c-axis). In this direction, B_{c} is about one order of magnitude smaller than the value measured in the macrostructure ($B_{\mathrm{c},\perp} \sim$ 6mT). The temperature dependence of $B_{\mathrm{c},\perp}$ is linear (Figure 3.b in blue), like in the case of the macroscopic crystal. This was expected since there is no confinement effect in the $ab-$ plane. Nevertheless, we measured two different linear behaviors of $B_{\mathrm{c},\perp}$, crossing each other at about 335 mK (see also SI-9 for different set of contacts). The low temperature linear dependence corresponds to $\xi = 180$ nm and a T_{c} of 392 mK, substantially larger than the $T_{\mathrm{c}} \simeq 360$ mK measured. The high temperature behavior corresponds to $T_{\mathrm{c}} = 360$ mK, in good agreement with the measured value, and to $\xi = 120$ nm. An explanation of this unexpected crossover is still lacking so far.

When tilting the magnetic field by 90 °, we can extract the temperature dependence of $B_{\mathrm{c},||}$

(within a 1.1 °misalignment as shown below). Two important differences can be noticed with respect to the 3D case. Firstly, the amplitude of the critical field is about 30 times larger when pointing into the plane than perpendicularly to it. Taking the full angular dependence into account, so as to correct the misalignment, the ratio between in-plane and out-of-plane critical fields amounts up to 57. The in-plane critical field reaches 240 mT, four times larger than the B_c of a macroscopic structure. This value remains below the Pauli paramagnetic limit[70,71] $B_\mathrm{p} \simeq 1.84 T_\mathrm{c} \simeq$ 660 mT. Secondly, the temperature dependence of $B_{\mathrm{c},\|}$ is not linear. Rather, it follows the 2D phenomenological Ginzburg-Landau theory[72] valid for $\xi > d$ where d is the thickness of the superconductor:

$$B_{\mathrm{c},\|}(T) = \frac{\Phi_0 \sqrt{12}}{2\pi\xi(0)d}\sqrt{1-\frac{T}{T_c}}, \tag{2}$$

Taking into account a misalignment of 1.1°, it is possible to fit the temperature dependence of $B_{\mathrm{c},\|}$ (see SI-11). A very good agreement between the fit and the experimental data is obtained (Figure 3.b) and yields the values for $T_\mathrm{c} = 363$ mK, $\xi = 90$ nm and $d = 52$ nm. The thickness is in very good agreement with the value measured by atomic force microscopy d_AFM =57 nm, indicating that superconductivity cannot be attributed to surface states but rather to bulk states. Indubitably, this temperature dependence points to the 2D nature of the superconductivity. The value of ξ is between the value found in macroscopic structure and that given by the temperature dependence of $B_{\mathrm{c},\perp}$. The discrepancy between the values of ξ extracted from $B_{\mathrm{c},\perp}(T)$ and from $B_{\mathrm{c},\|}(T)$ are reasonable and might result from in-plane anisotropy as already measured in MoTe_2[66].

The angular dependence $B_\mathrm{c}(\theta)$ with θ being the angle between the magnetic field and the perpendicular axis of the flake, can give further evidence of the low dimensionality of the superconducting state. As shown by the Tinkham model, and contrary to the 3D anisotropic mass model derived from the Ginzburg-Landau theory, the 2D nature of the superconductivity is indicated by a cusp-like peak in $B_\mathrm{c}(\theta)$ at $\theta = 90°$(corresponding to an in-plane field). The 3D and 2D angular dependences are respectively given by

$$\left(\frac{B_\mathrm{c}(\theta)\cos(\theta-\theta_0)}{B_{\mathrm{c},\perp}}\right)^2 + \left(\frac{B_\mathrm{c}(\theta)\sin(\theta-\theta_0)}{B_{\mathrm{c},\|}}\right)^2 = 1, \text{ and} \tag{3}$$

$$\left|\frac{B_\mathrm{c}(\theta)\cos(\theta-\theta_0)}{B_{\mathrm{c},\perp}}\right| + \left(\frac{B_\mathrm{c}(\theta)\sin(\theta-\theta_0)}{B_{\mathrm{c},\|}}\right)^2 = 1, \tag{4}$$

where θ_0 stands for the misalignment angle. In Figure 3.c, a very sharp peak of B_c is measured at $\theta \simeq 90°$ with a ratio between the largest and the smallest critical field that can be as large as 57. As it can be seen in the inset in the Figure 3.c, the sharpness of the peak allows us to measure very precisely θ_0 and we found $\theta_0 = 1.1°$ in our sample. Due to the very strong anisotropy measured in the sample, such a minimal misalignment induces a reduction of about 25% of B_c at $\theta = 0°$and the misalignment has to be taken into account as mentioned above. Importantly, a cusp-like angular dependence can be evidenced in the inset in Figure 3.c, which also presents 2D (red) and 3D (blue) fits of $B_\mathrm{c}(\theta)$. Whereas the 2D model fits very well the experimental data, a clear departure from the 3D model can be seen in the inset.

BKT Transition. Despite the large thickness of our $\mathrm{PtBi_2}$ sample, the angular and temperature dependences of B_c give clear evidence of 2D superconductivity, opening the way to the observation of a BKT transition. The signatures of such a phase transition can be measured in $V(I)$ characteristics at different temperatures and in the temperature dependence of the resistance $R(T)$.

As shown in Figure 4.a, due to the finite critical current, the $V(I)$ characteristics become non-linear at low bias and low temperature, with a temperature-dependent power law[73] as:

$$V \propto I^{a(T)} \text{ with } a(T) = 1 + \pi J_{\text{S}}(T)/T, \tag{5}$$

where J_{S} is the superfluid density and the exponent a is equal to 1 at $T \gtrsim T_{\text{c}}$, as well as at high current bias ($I \gg I_{\text{c}}$) for $T \lesssim T_{\text{c}}$. In a BKT transition, $a(T)$ at $I \sim I_{\text{c}}$ slowly increases when T decreases below T_{c} and it largely exceeds 1 at temperatures much below the BKT temperature $T_{\text{BKT}} < T_{\text{c}}$. At the BKT transition, $\pi J_{\text{S}}(T_{\text{BKT}})/T_{\text{BKT}} = 2$ so that $a(T_{\text{BKT}}) = 3$. Considering the $V(I)$ characteristics measured in our flake above and below T_{c}, we observe a non-ohmicity ($a(T) > 1$) when $T \lesssim T_{\text{c}}$ (see Figure 4.a and 4.b). In a logarithmic plot, the $V(I)$ shows a cubic power law for $T_{\text{BKT}} \simeq 310$ mK (Figure 4.a). A confirmation of the BKT transition temperature can be done by plotting $a(T) = d\log V/d\log I$ as a function of the bias DC-current as shown in Figure 4.b where $a(T)$ reaches 3 for $T = T_{\text{BKT}} \simeq 310$ mK.

In order to confirm that a BKT transition occurs in our sample, we focused on the temperature dependence of the resistance of our exfoliated thin film. Following Halperin and Nelson theory[11], Benfatto *et al.* took, in absence of inhomogeneities and size effect, a temperature dependence of the resistance for $T \gtrsim T_{\text{BKT}}$ given by $R(T)/R_{\text{N}} = 1/[1 + (\Delta\sigma/\sigma_{\text{N}})]$ with[73]

$$\frac{\Delta\sigma}{\sigma_{\text{N}}} = \frac{4}{A^2}\left[\sinh\left(2\alpha\sqrt{\frac{T_{\text{c}} - T_{\text{BKT}}}{T - T_{\text{BKT}}}}\right)\right]^2 \tag{6}$$

where A is a number of the order of unity and α is the scale of the vortex-core energy, which may deviate from its regular value $\alpha = 1$. The fit of the experimental data can reproduce the temperature dependence but gives $T_{\text{BKT}} \simeq 200$ mK, much below the value given by the $V(I)$ characteristics.

Fixing T_{BKT} to 310 mK, as given by $V(I)$ measurements, no reasonable fit could be obtained (see the red dashed line in Figure 4.c for the best fit).

A model that accounts for spatial inhomogeneities was proposed in Ref. 73, where a Gaussian distribution of the critical current, or equivalently, of T_{BKT}, is introduced in the Halperin-Nelson model. We have now

$$\frac{R(T)}{R_{\mathrm{N}}} = \frac{1}{\sqrt{2\pi}\delta} \int \exp\left(-\frac{(t - T_{\mathrm{BKT}})^2}{2\delta^2}\right) \times \left(1 + \frac{4}{A^2}\left[\sinh\left(b\sqrt{\frac{t}{T-t}}\right)\right]^2\right)^{-1} dt \qquad (7)$$

with $b \simeq 2\alpha\sqrt{T_{\mathrm{BKT}}/(T_{\mathrm{c}} - T_{\mathrm{BKT}})}$. This model fits very well the experimental data even for T_{BKT} fixed at 310 mK, the value given by the $V(I)$ characteristics (see Figure 4.c) and we found $\delta \simeq 24$ mK, a minimal spread of the transition temperature. The parameter b and A are respectively 1.1 and 13, some typical values expected from the theory[73]. From the value of b, one can calculate the superconducting (BCS) transition temperature T_{c}, assuming that the vortex-core energy takes its conventional value ($\alpha = 1$). We found $T_{\mathrm{c}} = T_{\mathrm{BKT}} \times (1 + 4/b^2) = 410$ mK which corresponds to about 70% of the macroscopic crystal value, a reasonable decrease of T_{c} for an exfoliated flake.

3 Discussion

The role of inhomogeneities in the BKT transition can be seen in both the $V(I)$ characteristics as well as in the $R(T)$ dependence. In the latter, as discussed above, the tail of $R(T)$ can be very well fitted by a Gaussian distribution of the BKT transition temperature resulting from spatial inhomogeneities of the superconducting flake. The fit gives reasonable values of the different physical parameters. A consequence of inhomogeneities is the lack of universal jump of the superfluid density $J(T)$ and of $a(T)$ when $T \rightarrow T_{\text{BKT}}$. In an ideal homogeneous sample, the coefficient $a(T)$ should jump discontinuously at T_{BKT} from 1 for $T > T_{\text{BKT}}$ to 3 for $T \leq T_{\text{BKT}}$. Inhomogeneities smooth out the temperature dependence of $a(T)$[73]. This is indeed what we measured in our sample where the value of $a(T)$ slowly increases when the system goes through the BKT transition and no discontinuity of a could be evidenced (**??**.b). Importantly, the fit of $R(T)$ gives $\delta = 24$ mK, a value that compares very well with the spatial distribution of T_{BKT} measured in different sets of contact pairs with $T_{\text{BKT}} = 310 - 340$ mK (see SI-10).

We also note that the ratio $B_{\text{c},\|}/B_{\text{c},\perp}$ is found to be very large, up to 57, which is unusual for such thick superconducting nanostructures ($d \simeq 60$ nm). This large ratio can be attributed first to the very long coherence length measured in our nanostructures ($\xi > d$) and second to the change of slope measured in $B_{\text{c},\perp}(T)$ with a discontinuity of $dB_{\text{c},\perp}/dT$ at $T \simeq 335$ mK. Such a discontinuity is present for all the contact pairs measured in this nanostructure. The very large ratio measured and more particularly the large value of $B_{\text{c},\|}$ (as compared to $k_{\text{B}}T_{\text{c}}$) for such a large thickness makes exfoliated flakes of PtBi_2 single crystal a very promising candidate to study the 2D superconductivity beyond the Pauli limit[70,71], provided that the thickness is reduced further in order to weaken or suppress any orbital depairing effect on the superconductivity.

The discovery of both the non-trivial topology of the band structure and the low dimensional superconductivity sheds new light on PtBi_2, a material that was previously known for its very large linear magnetoresistance, its large spin-orbit coupling and the prediction of triply degenerate points in its band structure. Together with MoTe_2[66], it appears to be the only semimetal exhibiting

Weyl physics and 2D superconductivity. Beyond topological superconductivity, the very strong spin-orbit coupling coupled to the superconducting transition is of particular interest in the search for unconventional pairing in superconductors and might favor, for instance, the presence of FFLO superconducting states.

The evidence of a BKT transition in a 60 nm thick flake makes of $PtBi_2$ a remarkable system. This very large thickness is highly unusual for the observation of 2D superconductivity. To our knowledge and excluding the case of layered superconductors, our flake is 5 times thicker than the thickest 2D superconductor reported so far[60]. The origin of the reduced dimensionality cannot be attributed to any surface effect or to any layered nature of $PtBi_2$ since we established the 3D nature of the superconductivity in macroscopic single crystals and since the effective superconducting thickness given by the fit of $B_{\mathrm{c},||}(T)$ compares very well with the geometrical thickness measured by AFM. Apart from promising properties of 2D superconductor that might be observed in thinner structures, such as the increase of $B_{\mathrm{c},||}$ well beyond the Pauli limit, the large thickness is also an indication of a very robust signature of the usually fragile 2D superconducting state. $PtBi_2$ might be therefore a simple and privileged platform for studying 2D superconductivity and the BKT transition.

4 Methods

DFT calculation. The calculation of the Weyl nodes and of the surface Fermi surface were performed based on a tightbinding model obtained by constructing Wannier functions with the projective technique implemented in the FPLO code. The model includes the orbitals Bi 6p, Pt 6s and Pt 5d.

To evaluate the robusness of the Weyl nodes, we also performed calculations for the crystal structure reported in Ref. 74. These confirm the presence of Weyl nodes albeit, in this case, they are found at higher energy, 96 meV. Noteworthy, between these two crystal structures, the values of a and c differ in less than 0.1% while differences in the Bi coordinates lead to a van der Waals gap (zvdW) 3% smaller in our refinement. A third calculation based on an artificially enlarged zvdW in our structural model yields the Weyl nodes at 79 meV indicating that, in fact, zvdW controls to a large extent the Weyl node energy.

Point contact measurements. The contacts where made by mechanically touching the edge of the sample with the wire of the noble metal. The differential resistance (dV/dI) of the contacts was recorded via lock-in technique in a quasi four probe configuration. Latter was achieved by soldering one pair of a current-potential wiring to the copper sample clamp and another pair to the counter electrode (Ag, Au or Cu).

Measurements techniques. For the superconductivity in macroscopic crystals, DC sources were used in a delta mode, a method particularly adapted to the measurement of low resistance samples. The measurements of nanostructures were done using standard lock-in amplifier techniques at low frequency ($f < 200$ Hz).

Nanostructure fabrication. The exfoliation was made on Si/SiO$_2$ substrates, with 290 nm thickness of oxide, to enhance optical contrast. The exfoliated structures were then contacted by standard electron-beam lithography procedure, with Cr-Au contacts. The structure we measured for this work, which can be seen in the supplementary information, has a thickness of 60nm, for a lateral size of about 10μm.

Definition of the critical parameters. The critical temperature T_c is defined in this work as the temperature for which the resistance becomes half of the resistance in the normal state R_N. Similarly, the critical field B_c and the critical current I_c are defined by $R(T_\mathrm{c}, B_\mathrm{c}, I_\mathrm{c}) = R_\mathrm{N}/2$ respectively.

1. Shalnikov, A. Superconducting thin films. *Nature* **142**, 74–74 (1938). URL https://doi.org/10.1038/142074a0.
2. Mermin, N. D. & Wagner, H. Absence of ferromagnetism or antiferromagnetism in one- or two-dimensional isotropic heisenberg models. *PRL* **17**, 1133–1136 (1966). URL https://link.aps.org/doi/10.1103/PhysRevLett.17.1133.
3. Hohenberg, P. C. Existence of long-range order in one and two dimensions. *Phys. Rev.* **158**, 383–386 (1967). URL https://link.aps.org/doi/10.1103/PhysRev.158.383.
4. Mermin, N. D. Absence of ordering in certain classical systems. *Journal of Mathematical Physics* **8**, 1061–1064 (1967). URL https://doi.org/10.1063/1.1705316.
5. Mermin, N. D. Crystalline order in two dimensions. *Phys. Rev.* **176**, 250–254 (1968). URL https://link.aps.org/doi/10.1103/PhysRev.176.250.

6. Coleman, S. There are no goldstone bosons in two dimensions. *Communications in Mathematical Physics* **31**, 259–264 (1973). URL https://doi.org/10.1007/BF01646487.

7. Berezinskii, V. L. Destruction of long-range order in one-dimensional and two-dimensional systems possessing a continuous symmetry group. ii. quantum systems. *Soviet Journal of Experimental and Theoretical Physics* **34**, 610 (1972). URL https://ui.adsabs.harvard.edu/abs/1972JETP...34..610B.

8. Kosterlitz, J. M. & Thouless, D. J. Long range order and metastability in two dimensional solids and superfluids. (application of dislocation theory). *Journal of Physics C: Solid State Physics* **5**, L124–L126 (1972). URL https://doi.org/10.1088%2F0022-3719%2F5%2F11%2F002.

9. Kosterlitz, J. M. & Thouless, D. J. Ordering, metastability and phase transitions in two-dimensional systems. *Journal of Physics C: Solid State Physics* **6**, 1181–1203 (1973). URL http://dx.doi.org/10.1088/0022-3719/6/7/010.

10. Minnhagen, P. The two-dimensional coulomb gas, vortex unbinding, and superfluid-superconducting films. *Rev. Mod. Phys.* **59**, 1001–1066 (1987). URL https://link.aps.org/doi/10.1103/RevModPhys.59.1001.

11. Halperin, B. I. & Nelson, D. R. Resistive transition in superconducting films. *Journal of Low Temperature Physics* **36**, 599–616 (1979). URL https://doi.org/10.1007/BF00116988.

12. Doniach, S. & Huberman, B. A. Topological excitations in two-dimensional superconductors. *Phys. Rev. Lett.* **42**, 1169–1172 (1979). URL https://link.aps.org/doi/10.1103/PhysRevLett.42.1169.

13. Brun, C. *et al.* Remarkable effects of disorder on superconductivity of single atomic layers of lead on silicon. *Nature Physics* **10**, 444–450 (2014). URL https://doi.org/10.1038/nphys2937.

14. Brun, C., Cren, T. & Roditchev, D. Review of 2d superconductivity: the ultimate case of epitaxial monolayers. *Superconductor Science and Technology* **30**, 013003 (2016). URL http://dx.doi.org/10.1088/0953-2048/30/1/013003.

15. Hebard, A. F. & Fiory, A. T. Critical-exponent measurements of a two-dimensional superconductor. *Phys. Rev. Lett.* **50**, 1603–1606 (1983). URL https://link.aps.org/doi/10.1103/PhysRevLett.50.1603.

16. Hsu, J. W. P. & Kapitulnik, A. Superconducting transition, fluctuation, and vortex motion in a two-dimensional single-crystal nb film. *PRB* **45**, 4819–4835 (1992). URL https://link.aps.org/doi/10.1103/PhysRevB.45.4819.

17. Qin, S., Kim, J., Niu, Q. & Shih, C.-K. Superconductivity at the two-dimensional limit. *Science* **324**, 1314–1317 (2009). URL https://science.sciencemag.org/content/324/5932/1314. https://science.sciencemag.org/content/324/5932/1314.full.pdf.

18. Zhang, T. *et al.* Superconductivity in one-atomic-layer metal films grown on si(111). *Nature Physics* **6**, 104–108 (2010). URL https://doi.org/10.1038/nphys1499.

19. Zhao, W. *et al.* Evidence for berezinskii–kosterlitz–thouless transition in atomically flat two-dimensional pb superconducting films. *Solid State Communications* **165**, 59 – 63 (2013). URL http://www.sciencedirect.com/science/article/pii/S0038109813001993.

20. Zhang, H.-M. *et al.* Detection of a superconducting phase in a two-atom layer of hexagonal ga film grown on semiconducting gan(0001). *Phys. Rev. Lett.* **114**, 107003 (2015). URL https://link.aps.org/doi/10.1103/PhysRevLett.114.107003.

21. Matetskiy, A. V. *et al.* Two-dimensional superconductor with a giant rashba effect: One-atom-layer tl-pb compound on si(111). *PRL* **115**, 147003 (2015). URL https://link.aps.org/doi/10.1103/PhysRevLett.115.147003.

22. Ge, J.-F. *et al.* Superconductivity above 100 k in single-layer fese films on doped srtio3. *Nature Materials* **14**, 285–289 (2015). URL https://doi.org/10.1038/nmat4153.

23. Hetel, I., Lemberger, T. R. & Randeria, M. Quantum critical behaviour in the superfluid density of strongly underdoped ultrathin copper oxide films. *Nature Physics* **3**, 700–702 (2007). URL https://doi.org/10.1038/nphys707.

24. Staley, N. E. *et al.* Electric field effect on superconductivity in atomically thin flakes of nbse$_2$. *Phys. Rev. B* **80**, 184505 (2009). URL https://link.aps.org/doi/10.1103/PhysRevB.80.184505.

25. Jiang, D. *et al.* High-tc superconductivity in ultrathin bi2sr2cacu2o8+x down to half-unit-cell thickness by protection with graphene. *Nature Communications* **5**, 5708 (2014). URL https://doi.org/10.1038/ncomms6708.

26. Cao, Y. *et al.* Quality heterostructures from two-dimensional crystals unstable in air by their assembly in inert atmosphere. *Nano Lett.* **15**, 4914–4921 (2015). URL https://doi.org/10.1021/acs.nanolett.5b00648.

27. Xi, X. *et al.* Strongly enhanced charge-density-wave order in monolayer nbse2. *Nature Nanotechnology* **10**, 765–769 (2015). URL https://doi.org/10.1038/nnano.2015.143.

28. Reyren, N. *et al.* Superconducting interfaces between insulating oxides. *Science* **317**, 1196 (2007). URL http://science.sciencemag.org/content/317/5842/1196.abstract.

29. Ueno, K. *et al.* Electric-field-induced superconductivity in an insulator. *Nature Materials* **7**, 855–858 (2008). URL https://doi.org/10.1038/nmat2298.

30. Ye, J. T. *et al.* Liquid-gated interface superconductivity on an atomically flat film. *Nature Materials* **9**, 125–128 (2010). URL https://doi.org/10.1038/nmat2587.

31. Cao, Y. *et al.* Unconventional superconductivity in magic-angle graphene superlattices. *Nature* **556**, 43 (2018). URL http://dx.doi.org/10.1038/nature26160.

32. Miller, J. L. Unconventional superconductivity discovered in graphene bilayers. *Physics Today* **71**, 15–19 (2018). URL https://doi.org/10.1063/PT.3.3913.

33. Fatemi, V. *et al.* Electrically tunable low-density superconductivity in a monolayer topological insulator. *Science* **362**, 926–929 (2018). URL https://science.sciencemag.org/content/362/6417/926. https://science.sciencemag.org/content/362/6417/926.full.pdf.

34. Sajadi, E. *et al.* Gate-induced superconductivity in a monolayer topological insulator. *Science* **362**, 922–925 (2018). URL https://science.sciencemag.org/content/362/6417/922. https://science.sciencemag.org/content/362/6417/922.full.pdf.

35. Edel'shtein, V. M. Characteristics of the cooper pairing in two-dimensional noncentrosymmetric electron systems. *Soviet Physics - JETP (English Translation)* **68**, 1244–1249 (1989). URL http://inis.iaea.org/search/search.aspx?orig_q=RN:22082571.

36. Gor'kov, L. P. & Rashba, E. I. Superconducting 2d system with lifted spin degeneracy: Mixed singlet-triplet state. *PRL* **87**, 037004 (2001). URL https://link.aps.org/doi/10.1103/PhysRevLett.87.037004.

37. Kozii, V. & Fu, L. Odd-parity superconductivity in the vicinity of inversion symmetry breaking in spin-orbit-coupled systems. *Phys. Rev. Lett.* **115**, 207002 (2015). URL https://link.aps.org/doi/10.1103/PhysRevLett.115.207002.

38. Fulde, P. & Ferrell, R. A. Superconductivity in a strong spin-exchange field. *Phys. Rev.* **135**, A550–A563 (1964). URL https://link.aps.org/doi/10.1103/PhysRev.135.A550.

39. Larkin, A. I. & Ovchinnikov, I. U. N. Inhomogeneous state of superconductors(production of superconducting state in ferromagnet with fermi surfaces, examining green function). *Soviet Physics-JETP* **20**, 762–769 (1965).

40. Michaeli, K., Potter, A. C. & Lee, P. A. Superconducting and ferromagnetic phases in $\mathrm{srtio}_3/\mathrm{laalo}_3$ oxide interface structures: Possibility of finite momentum pairing. *Phys. Rev. Lett.* **108**, 117003 (2012). URL https://link.aps.org/doi/10.1103/PhysRevLett.108.117003.

41. Mayaffre, H. *et al.* Evidence of andreev bound states as a hallmark of the fflo phase in κ-(bedt-ttf)2cu(ncs)2. *Nature Physics* **10**, 928 (2014). URL https://doi.org/10.1038/nphys3121.

42. Kinnunen, J. J., Baarsma, J. E., Martikainen, J.-P. & Törmä, P. The fulde-ferrell-larkin-ovchinnikov state for ultracold fermions in lattice and harmonic potentials: a review. *Reports on Progress in Physics* **81**, 046401 (2018). URL http://dx.doi.org/10.1088/1361-6633/aaa4ad.

43. Song, K. W. & Koshelev, A. E. Quantum fflo state in clean layered superconductors. *Phys. Rev. X* **9**, 021025 (2019). URL https://link.aps.org/doi/10.1103/PhysRevX.9.021025.

44. Cho, G. Y., Bardarson, J. H., Lu, Y.-M. & Moore, J. E. Superconductivity of doped weyl semimetals: Finite-momentum pairing and electronic analog of the ^{3}he-a phase. *Phys. Rev. B* **86**, 214514 (2012). URL https://link.aps.org/doi/10.1103/PhysRevB.86.214514.

45. Wei, H., Chao, S.-P. & Aji, V. Odd-parity superconductivity in weyl semimetals. *Phys. Rev. B* **89**, 014506 (2014). URL https://link.aps.org/doi/10.1103/PhysRevB.89.014506.

46. Hosur, P., Dai, X., Fang, Z. & Qi, X.-L. Time-reversal-invariant topological superconductivity in doped weyl semimetals. *Phys. Rev. B* **90**, 045130 (2014). URL https://link.aps.org/doi/10.1103/PhysRevB.90.045130.

47. Bednik, G., Zyuzin, A. A. & Burkov, A. A. Superconductivity in weyl metals. *Phys. Rev. B* **92**, 035153 (2015). URL https://link.aps.org/doi/10.1103/PhysRevB.92.035153.

48. Kim, Y., Park, M. J. & Gilbert, M. J. Probing unconventional superconductivity in inversion-symmetric doped weyl semimetal. *Phys. Rev. B* **93**, 214511 (2016). URL https://link.aps.org/doi/10.1103/PhysRevB.93.214511.

49. Zhou, T., Gao, Y. & Wang, Z. D. Superconductivity in doped inversion-symmetric weyl semimetals. *Phys. Rev. B* **93**, 094517 (2016). URL https://link.aps.org/doi/10.1103/PhysRevB.93.094517.

50. Hao, L., Wang, R., Hosur, P. & Ting, C. S. Larkin-ovchinnikov state of superconducting weyl metals: Fundamental differences between restricted and extended pairings in k-space. *Phys. Rev. B* **96**, 094530 (2017). URL https://link.aps.org/doi/10.1103/PhysRevB.96.094530.

51. Zhou, T., Gao, Y. & Wang, Z. D. Resolving different pairing states in weyl superconductors through the single-particle spectrum. *Phys. Rev. B* **98**, 024515 (2018). URL https://link.aps.org/doi/10.1103/PhysRevB.98.024515.

52. Yang, X. *et al.* Giant linear magneto-resistance in nonmagnetic ptbi2. *Appl. Phys. Lett.* **108**, 252401 (2016). URL https://doi.org/10.1063/1.4954272.

53. Gao, W. *et al.* Extremely large magnetoresistance in a topological semimetal candidate pyrite ptbi_2. *Phys. Rev. Lett.* **118**, 256601 (2017). URL https://link.aps.org/doi/10.1103/PhysRevLett.118.256601.

54. Feng, Y. *et al.* Rashba-like spin splitting along three momentum directions in trigonal layered ptbi2. *Nature Communications* **10**, 4765 (2019). URL https://doi.org/10.1038/s41467-019-12805-2.

55. Gao, W. *et al.* A possible candidate for triply degenerate point fermions in trigonal layered ptbi2. *Nature Communications* **9**, 3249 (2018). URL https://doi.org/10.1038/s41467-018-05730-3.

56. Thirupathaiah, S. *et al.* Sixfold fermion near the Fermi level in cubic PtBi2. *arXiv e-prints* arXiv:2006.08642 (2020). 2006.08642.

57. Nie, X.-A. *et al.* Robust hot electron and multiple topological insulator states in ptbi2. *ACS Nano* (2020). URL https://doi.org/10.1021/acsnano.9b09564.

58. Baity, P. G., Shi, X., Shi, Z., Benfatto, L. & Popović, D. Effective two-dimensional thickness for the berezinskii-kosterlitz-thouless-like transition in a highly underdoped $\mathrm{la}_{2-x}\mathrm{sr}_x\mathrm{cuo}_4$. *Phys. Rev. B* **93**, 024519 (2016). URL https://link.aps.org/doi/10.1103/PhysRevB.93.024519.

59. Guo, J. G. *et al.* Quasi-two-dimensional superconductivity from dimerization of atomically ordered aute(2)se(4/3) cubes. *Nature communications* **8**, 871–871 (2017). URL https://www.nature.com/articles/s41467-017-00947-0.

60. Mondal, M. *et al.* Role of the vortex-core energy on the berezinskii-kosterlitz-thouless transition in thin films of nbn. *Phys. Rev. Lett.* **107**, 217003 (2011). URL https://link.aps.org/doi/10.1103/PhysRevLett.107.217003.

61. Qi, Y. *et al.* Superconductivity in weyl semimetal candidate mote2. *Nature Communications* **7**, 11038 (2016). URL http://dx.doi.org/10.1038/ncomms11038.

62. Li, Y. *et al.* Nontrivial superconductivity in topological mote(2-x) s (x) crystals. *Proceedings of the National Academy of Sciences of the United States of America* **115**, 9503–9508 (2018). URL https://www.pnas.org/content/115/38/9503.long.

63. Xing, Y. *et al.* Surface superconductivity in the type ii weyl semimetal tairte4. *Natl Sci Rev* **7**, 579–587 (2019). URL https://doi.org/10.1093/nsr/nwz204.

64. Baenitz, M., Schmidt, M., Suess, V., Felser, C. & Lüders, K. Superconductivity in weyl semimetal NbP: Bulk vs. surface. *Journal of Physics: Conference Series* **1293**, 012002 (2019). URL https://doi.org/10.1088%2F1742-6596%2F1293%2F1%2F012002.

65. van Delft, M. R. *et al.* Two- and three-dimensional superconducting phases in the weyl semimetal tap at ambient pressure. *Crystals* **10** (2020). URL https://www.mdpi.com/2073-4352/10/4/288.

66. Cui, J. *et al.* Transport evidence of asymmetric spin-orbit coupling in few-layer superconducting 1td-mote2. *Nature Communications* **10**, 2044 (2019). URL https://doi.org/10.1038/s41467-019-09995-0.

67. Shipunov, G. *et al.* Polymorphic ptbi$_2$ — candidate for topological superconductivity (2020). URL https://ui.adsabs.harvard.edu/abs/2020arXiv200203976S.

68. Koepernik, K. & Eschrig, H. Full-potential nonorthogonal local-orbital minimum-basis band-structure scheme. *Phys. Rev. B* **59**, 1743–1757 (1999). URL https://link.aps.org/doi/10.1103/PhysRevB.59.1743.

69. Xing, L., Chapai, R., Nepal, R. & Jin, R. Topological behavior and zeeman splitting in trigonal ptbi2-x single crystals. *npj Quantum Materials* **5**, 10 (2020). URL https://doi.org/10.1038/s41535-020-0213-9.

70. Clogston, A. M. Upper limit for the critical field in hard superconductors. *PRL* **9**, 266–267 (1962). URL https://link.aps.org/doi/10.1103/PhysRevLett.9.266.

71. Chandrasekhar, B. S. A note on the maximum critical field of high field superconductors. *Appl. Phys. Lett.* **1**, 7–8 (1962). URL https://doi.org/10.1063/1.1777362.

72. Tinkham, M. *Introduction to superconductivity*. International series in pure and applied physics (McGraw-Hill, New York, 1975).

73. Benfatto, L., Castellani, C. & Giamarchi, T. Broadening of the berezinskii-kosterlitz-thouless superconducting transition by inhomogeneity and finite-size effects. *PRB* **80**, 214506 (2009). URL https://link.aps.org/doi/10.1103/PhysRevB.80.214506.

74. Kaiser, M., Baranov, A. I. & Ruck, M. Bi2pt(hp9) by low-temperature reduction of bi13pt3i7: Reinvestigation of the crystal structure and chemical bonding analysis. *Z. anorg. allg. Chem.* **640**, 2742–2746 (2014). URL https://doi.org/10.1002/zaac.201400331.

Acknowledgements

DLB and YuGN acknowledge funding by Volkswagen Foundation and are grateful for support by the National Academy of Sciences of Ukraine under project Φ4-19. JIF acknowledges the support from the Alexander von Humboldt Foundation. S.A. acknowledges financial support by the Deutsche Forschungsgemeinschaft (DFG) through the grant AS 523/4-1. J.D. acknowledges financial support by the Deutsche Forschungsgemeinschaft (DFG) through the SPP 1666 Topological Insulators program (Project DU 1376/2-2) and the Würzburg-Dresden Cluster of Excellence on Complexity and Topology in Quantum Matter - ct.qmat (EXC 2147, project-id 0392019). This project has received funding from the European Research Council (ERC) under the European

Unions Horizon 2020 research and innovation program (grant agreement No 647276-MARS-ERC-2014-CoG).

S1 - Fermi arcs

S2 - Temperature dependence

We present below the temperature dependence of the resistivity of a single macroscopic crystal exhibiting a residual resistance ratio of about 130.

S3 - Isotropy of the critical field in a macroscopic structure

S4 - Point contact measurements for different magnetic fields

As for the temperature, point-contact measurements show an enhanced local superconductivity in magnetic field likely due to local pressure, with indications of superconductivity at magnetic fields up to 1T. This value is six times larger than its bulk pressure value ($\approx$ 150 mT). The Figure 8 shows the enhancement of $B_{\rm c}$ at $T = 1.55$ K under the point contact for a magnetic field applied along the c-axis. The differential resistance (dV/dI) shows a zero-bias drop of almost 50$\%$ at 0 T and 1.55 K. At this temperature, a deviation from the ohmicity is observed at magnetic field up to 1 T, far beyond its bulk value.

S5 - Magnetoresistances of the nanostructure

The Figure 9 shows the magnetoresistances along the c-axis of the exfoliated crystal and for a field aligned in the a-b plane of the nanostructure. Measurements are done at $T \simeq 100$ mK and with an AC current of 5 μA. The perpendicular field can be swept up to $\pm$ 6T (the main coil of the 3D magnet system) whereas the parallel field could be swept only up to ± 2T. As for the macroscopic single crystal, the magnetoresistance is found to be almost linear and it is larger for a perpendicular field.

S6 - dV/dI for different contact pairs

Although the critical current is almost independent of the set of contacts considered, the exact shape of the differential resistance $dV/dI(I_{\mathrm{dc}})$ depends on the set considered. Some contacts shows a single peak shape whereas others have several peaks, as seen in the Figure 10. Moreover, this feature does not depend on the contacts used for current bias, as shown in the Figure 10 and Figure 11.

S7 - Critical current versus magnetic field

We measured the dependence of the $dV/dI(I_{\mathrm{dc}})$ with the magnetic field. In both directions $B_\perp$ and $B_{||}$, the critical current as defined in the main text ($R(I_{\mathrm{c}}) = R_{\mathrm{N}}/2$) is found to be proportional to the magnetic field with a larger sensitivity when the field is applied along the perpendicular direction. The results are indicated in Figure 10 for an in-plane magnetic field and in Figure 11 for an out-of-plane magnetic field. The diamond shape of $I_{\mathrm{c}}(B)$ in both direction indicates the proportionality of I_{c} with B.

All the dV/dI show a similar diamond shape like, including the multi-peaked differential resistance.

S8 - Critical current versus temperature

Data of the Figure 3.a presented in a two dimensional plot where the temperature dependency of the maximum of the dV/dI can be shown. Such a maximum is located at a dc current that corresponds almost exactly to the critical current so that the temperature evolution of the maximum also stands for the temperature dependency of I_{c}. The measurements are done by increasing the temperature by steps of 10 mK with a stabilization time of about 35 min between two $dV/dI(I_{\mathrm{dc}})$ sweeps so that the sample is very well thermalized.

S9 - temperature dependence of the critical field for another set of contacts

An example of the temperature dependence of $B_{\mathrm{c},\perp}$ is shown in black in the Figure 15 for a set of contacts indicating a discontinuous slope at about 330 mK, similar to the contact indicated in the main text (reproduced in blue). A set of contacts for which the accuracy of the measurement of $B_{\perp}$ is not enough to resolve the discontinuity of the slope is also indicated in red.

S10 - Temperature dependence of the resistance for different contacts with the fit to BKT

Three additional temperature dependences were measured and fitted with the BKT model for different set of contacts for voltage probes, source and drain. The results are shown in the Figure 14.

We summarize in the Table 1 the results obtained from the fit of the different experimental data with the Equation (7) in the main text. The value of the BCS critical temperature is calculated based on the parameter given by the fit of $R(T)$ assuming $\alpha = 1$. The value of T_{BKT} is fixed by the analysis of the $I(V)$ at different temperature as explained in the main text. We notice that the standard deviation of T_{BKT} is in very good agreement with the typical value obtained for δ.

S11 - determination of $B_{\mathrm{c}}(\theta, T)$

In order to extract the angle and temperature dependences of B_{c}, we replace in the solution of the Equation (4) the thermal depencency of $B_{\perp}(T)$ and $B_{\|}(T)$ given in the main text by Equation (2) and Equation (1) respectively. Such a solution is given by:

$$B_{\mathrm{c}}(\theta, T) = \frac{1}{2}\frac{B_{\|}(T)^2}{B_{\perp}(T)}\frac{|\cos\theta|}{\sin^2\theta}\left(\sqrt{1 + 4\frac{B_{\perp}(T)^2}{B_{\|}(T)^2}\frac{\sin^2\theta}{\cos^2\theta}} - 1\right) \tag{8}$$

where θ is the angle of the magnetic field with the perpendicular direction of the exfoliated flake.

Table 1: Results of the temperature dependence of the resistance from the normal regime down to below the BKT transition. The value of T_{BKT} is fixed by non-equilibrium measurements and α is assumed to be equal to unity whereas b, A and δ are the free parameters of the fit. T_{c} is calculated based on the value of b and α.

contact	T_{BKT} (mK)	parameter b	parameter A	α	δ (mK)	T_{c} (mK)
main text	310	1.15	13.4	1	23.6	412
blue	345	1.09	57.8	1	15.1	447
red	340	1.14	25.1	1	16.1	450
green	310	1.1	30.9	1	19.5	404

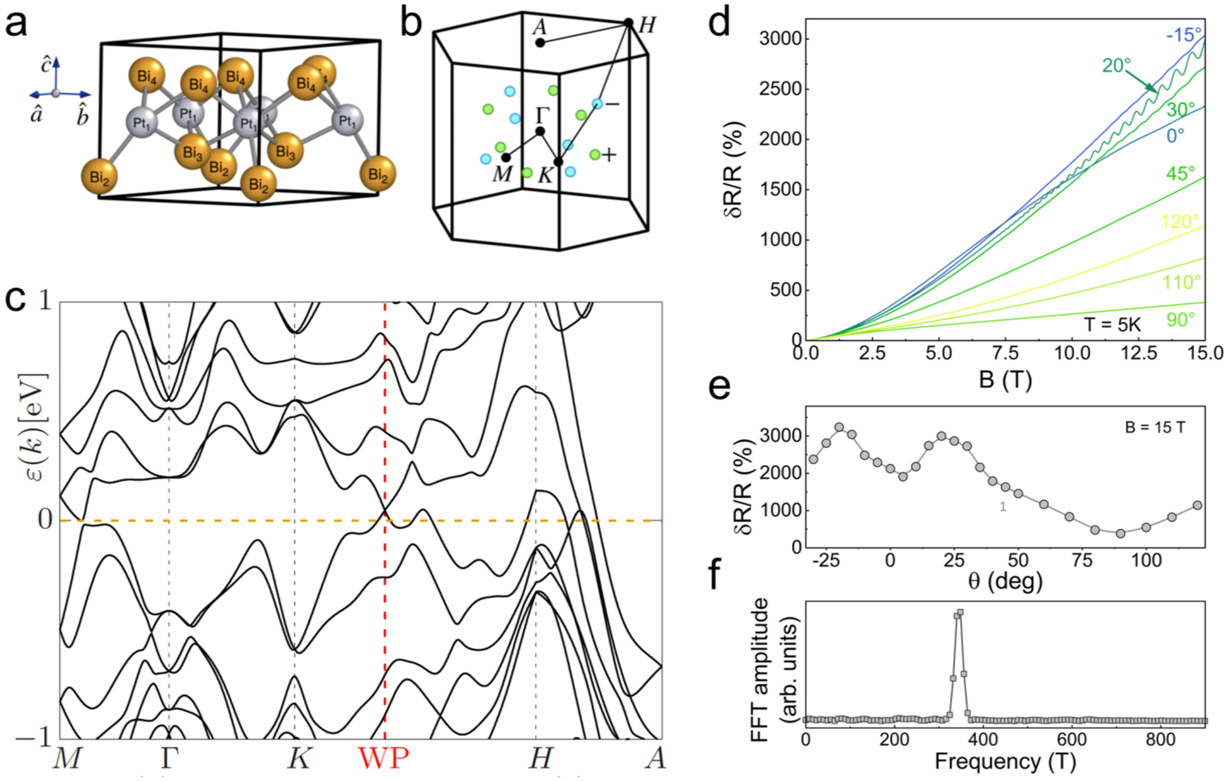

Figure 1: (a) Crystal structure of trigonal PtBi$_2$. (b) Brillouin zone. Green (light blue) points correspond to Weyl nodes of positive (negative) chirality. (c) Bandstructure along the path indicated in panel (b), which includes one of the Weyl nodes located at 48meV above the Fermi energy. (d) Magnetoresistance of a single crystal for different tilted angles θ of the field, θ being the angle between the magnetic field and the out-of-plane direction. (e) Angular dependence of the magnetoresistance at $B = 15$ T. (f) Fast Fourier Transform of the Shubnikov-de Haas oscillations in (d), for T=5K and $\theta = 20°$.

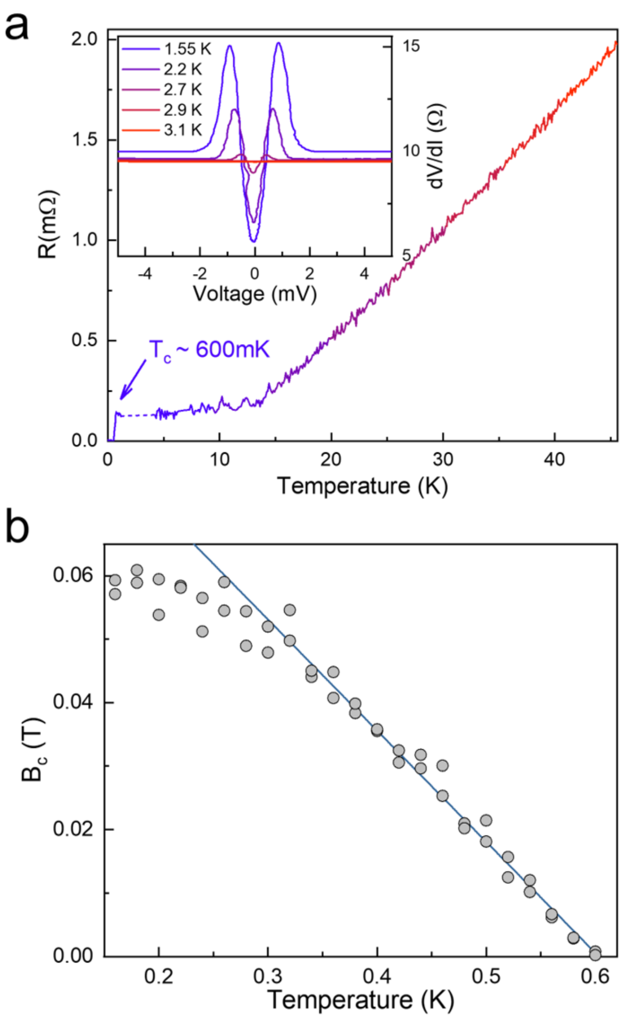

Figure 2: (a) The temperature dependence of the resistance of a single crystal for $T \leq 46$ K with a superconducting transition measured at $T_\mathrm{c} \simeq 600$ mK. The inset shows the differential resistance dV/dI as a function of the DC voltage in point contact measurements at different temperatures between 1.55 K and 3.1 K, indicating the onset of the superconductivity at about 2.5 K under point contact. (b) the temperature dependence of B_c (grey points) with the linear fit from Equation (1), leading to $\xi = 56$ nm at very low temperature.

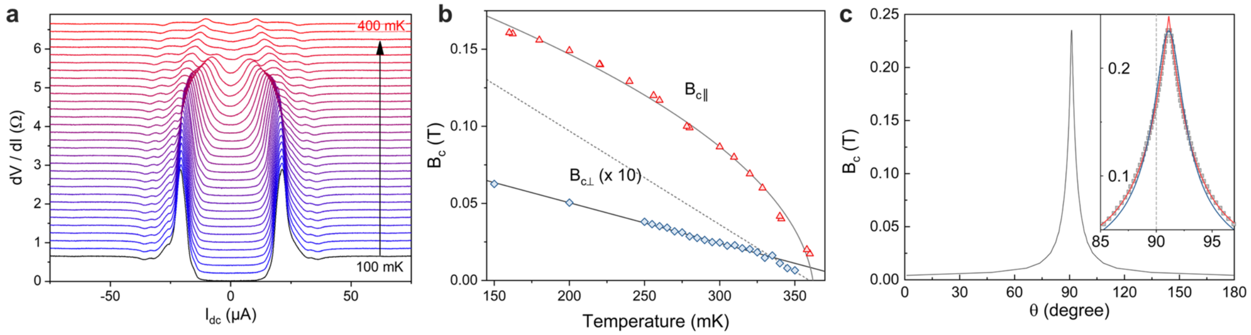

Figure 3: (a) Differential resistance dV/dI of the nanostructure as a function of the DC current at temperatures ranging regularly from 100 mK to 400 mK (the curves are shifted for better visibility). I_{c} was found to be about 20 μA. (b) temperature dependencies of the perpendicular ($B_{\mathrm{c},\perp}$) and planar ($B_{\mathrm{c},||}$) critical fields with their fit to the 2D theoretical model, including the misalignment measured in (c). (c) the angular dependence of the critical field at T =100 mK shows a sharp peak with a maximum corresponding to $\theta = 91.1$ °, indicating a 1.1° misalignment. Due to the sharpness of the peak, the $\theta = 0°$ is reduced by about 25% with respect to the true parallel critical field. Inset: the experimental data points (grey circles) of $B_{\mathrm{c}}(\theta)$ at $T = 100$ mK are fitted with the 3D Ginzburg-Landau model (blue line) and the 2D Tinkham model (red line). A better agreement is found for the 2D model.

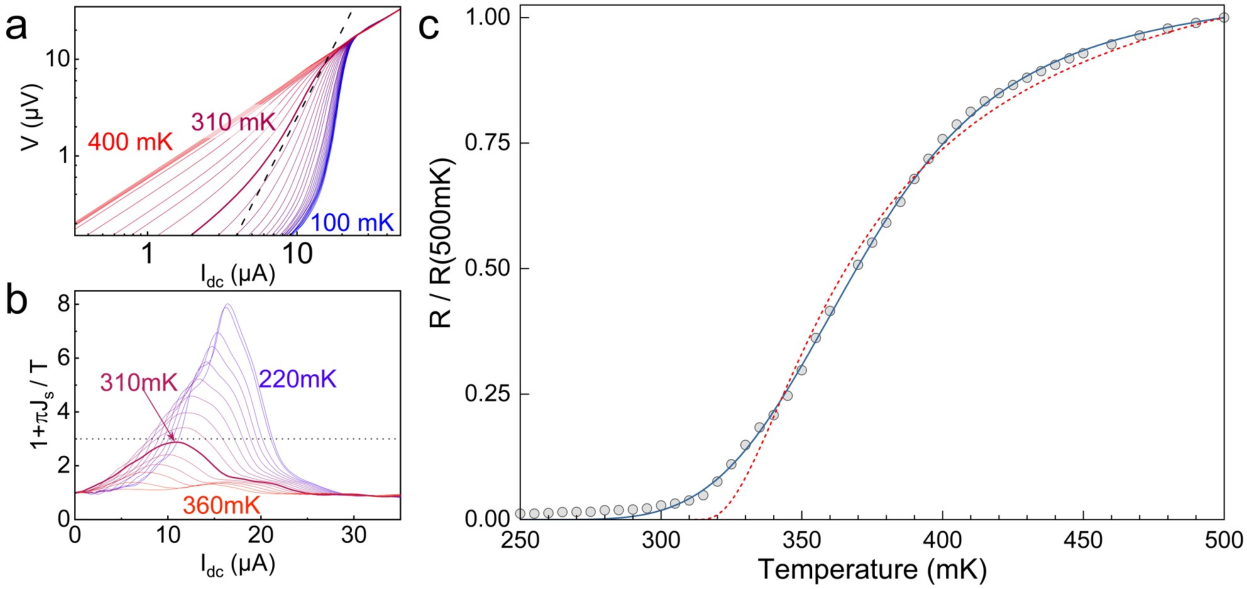

Figure 4: (a) $V(I)$ characteristics for different temperatures below T_{BKT} and above T_{c} in a logarithmic scale. The dashed line stands for $V \propto I^3$. (b) the same experimental data are plotted as $d\log V/d\log I(I) = a = 1 + \pi J_{\mathrm{S}}/T$ and the dashed line indicate the limit for which $a(T_{\mathrm{BKT}}) = 3$. Both inset indicate that $T_{\mathrm{BKT}} \simeq 310$ mK. (c) the temperaure dependence of the resistance of a PtBi_2 from the normal regime ($T \simeq 500$ mK) down to $T = 250$ mK $< T_{\mathrm{BKT}}$. The Halperin-Nelson theory (red dashed line) with $T_{\mathrm{BKT}} = 310$ mK is not able to fit the experimental data. Accounting for inhomogeneities, the fit with Benfatto's fomulae is in very good agreement with the experimental data for $T_{\mathrm{BKT}} = 310$ mK as found from the out-of-equilibrium measurements. The fit leads to $T_{\mathrm{c}} = 412$ mK and $\delta T_{\mathrm{BKT}} = 23$ mK. We note that we do not fit $R(T)/R_{\mathrm{N}}$ here, rather the equivalent quantity $R(T)/R(500mK) = R(T)/R_{\mathrm{N}} \times R_{\mathrm{N}}/R(500mK)$.

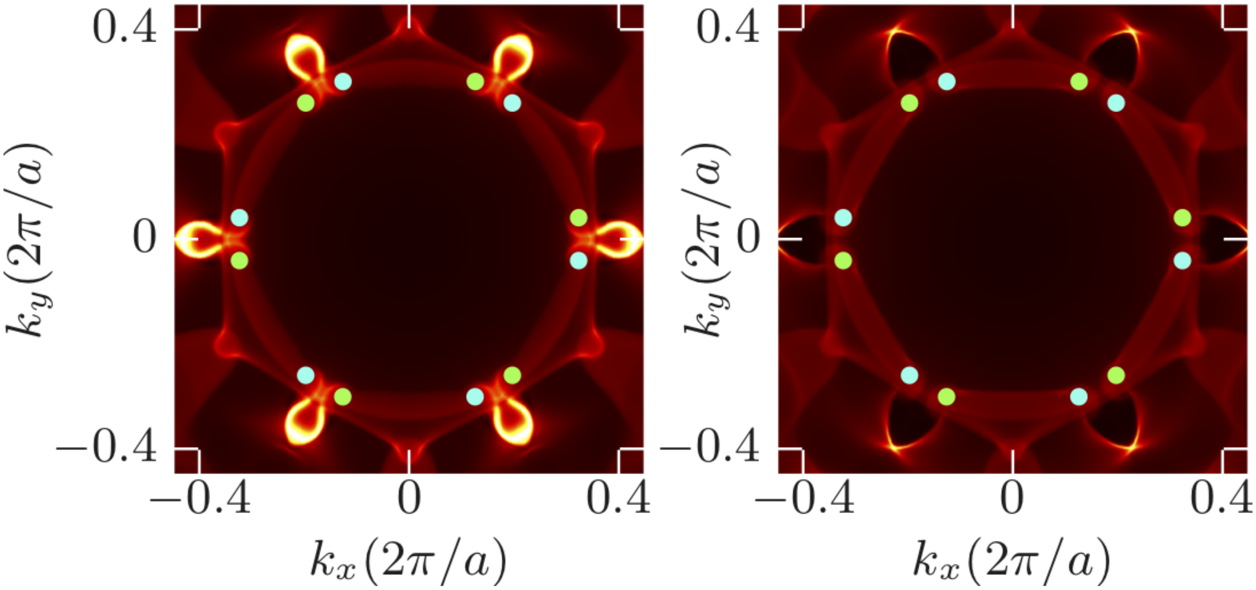

Figure 5: Surface Fermi surface corresponding to the charge neutrality point. Green (light blue) points correspond to the projection of Weyl nodes of positive (negative) chirality. Left: [001] Bi_2-terminated surface. Right: [001] Bi_4-terminated surface.

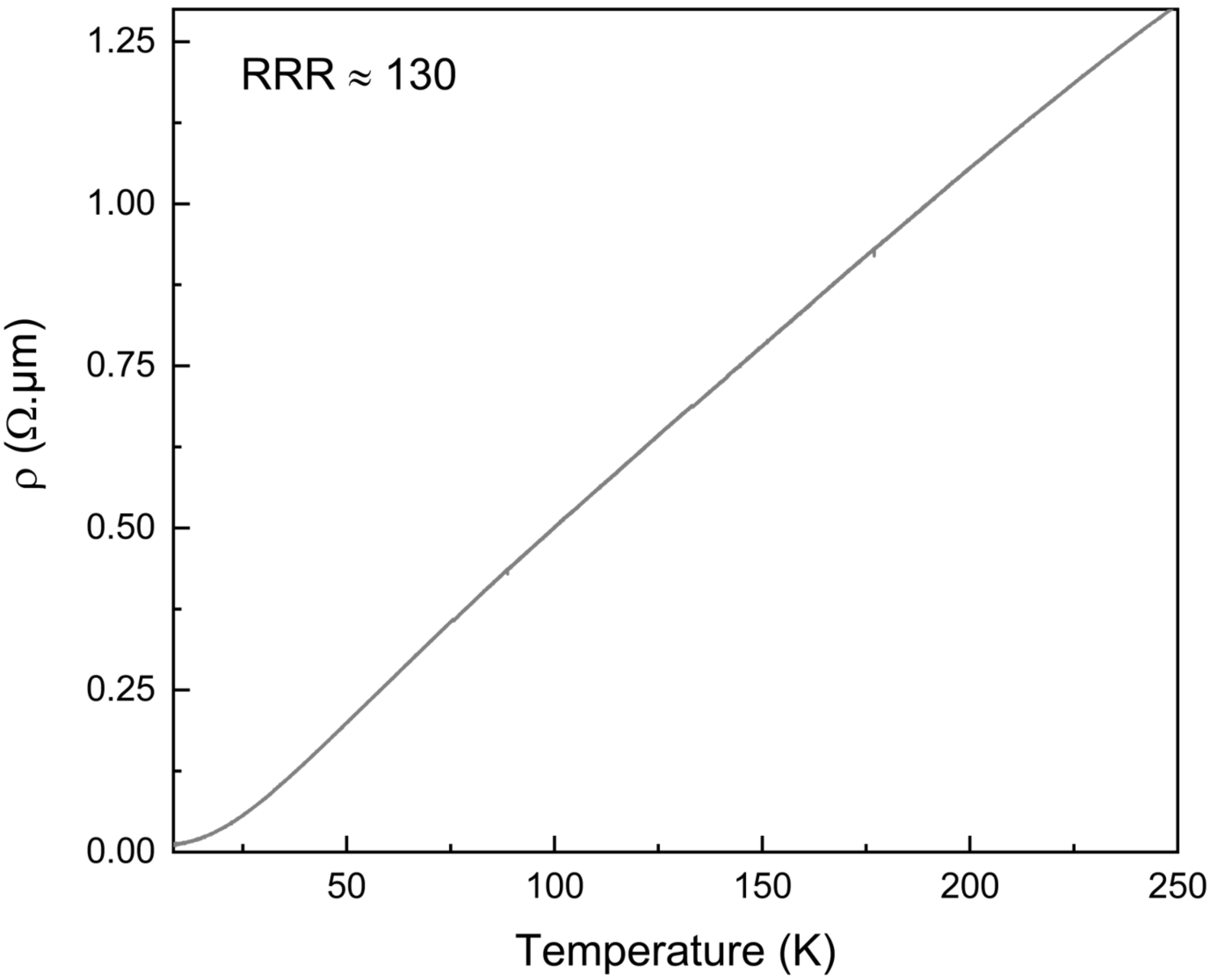

Figure 6: Temperature dependence of the resistivity of a macroscopic crystal between $T = 300$ K and 4.2 K.

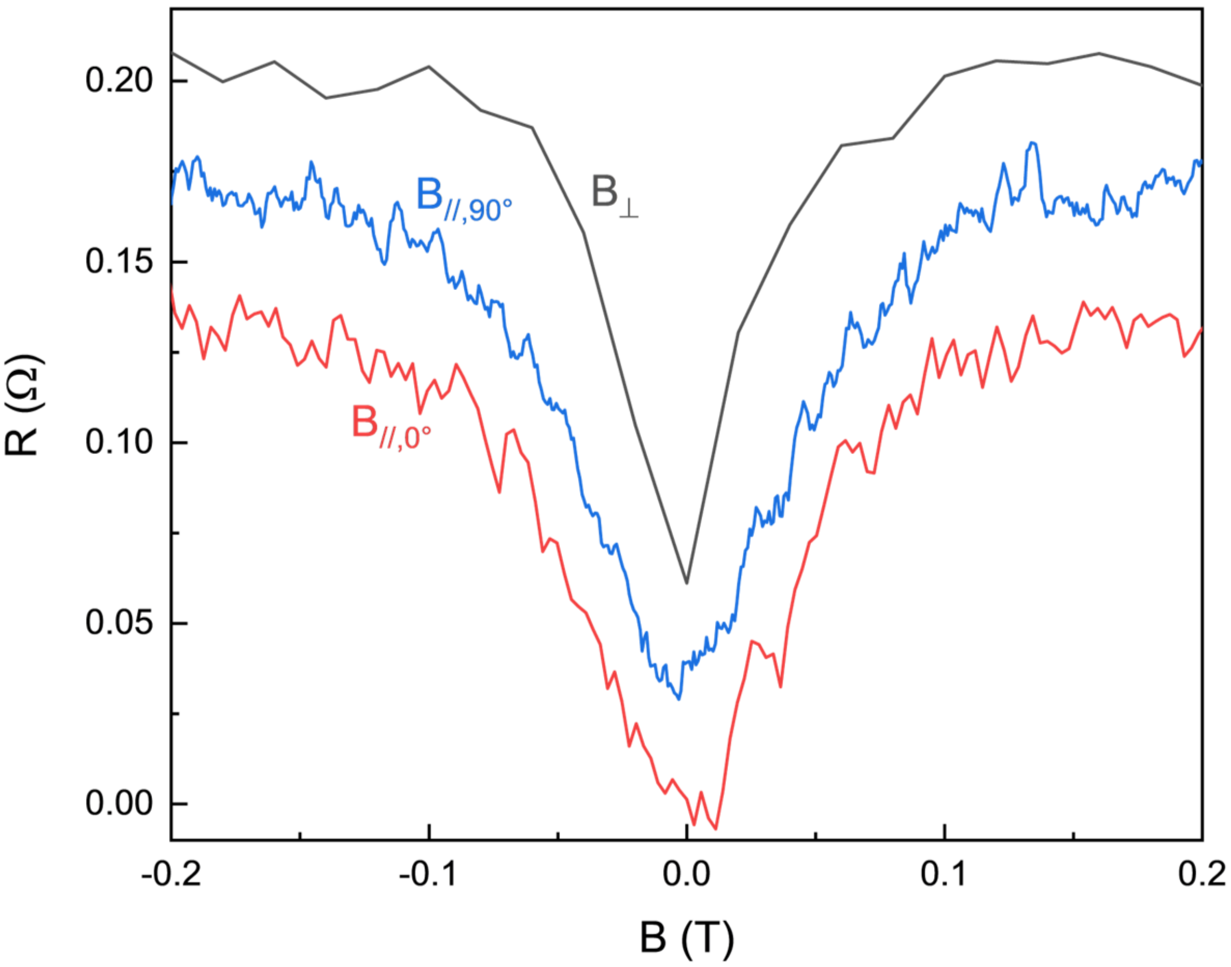

Figure 7: Magnetoresistance of a macroscopic crystal of $\mathrm{PtBi_2}$ with the magnetic field applied out-of-plane ($B_\perp$) or along the two perpendicular in-plane directions ($B_{\parallel,0}$ and $B_{\parallel,90}$) measured at low temperature ($T \sim 100$ mK). For the sake of clarity, the different curves are shifted.

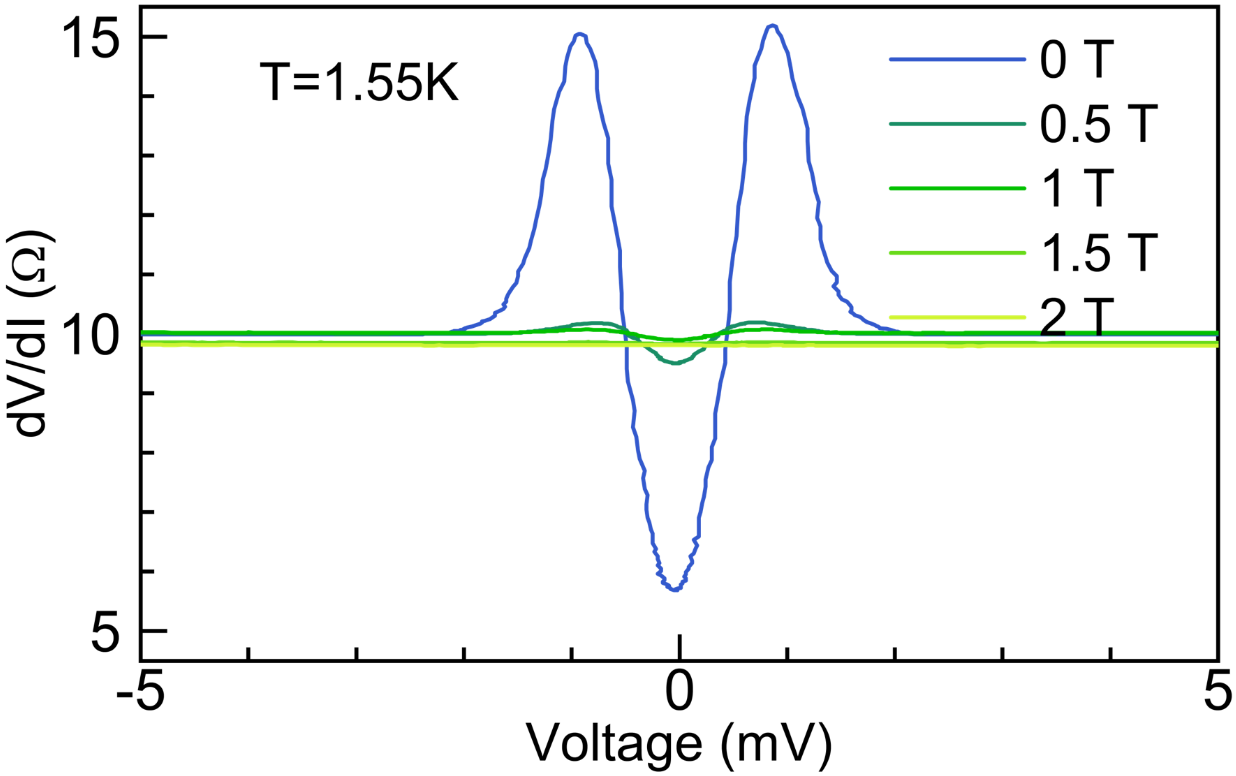

Figure 8: Differential resistance dV/dI as a function of the DC voltage in point contact measurements at different magnetic fields between 0 T and 2 T at 1.55 K, indicating the onset of the superconductivity below 1 T for $T = 1.55$ K.

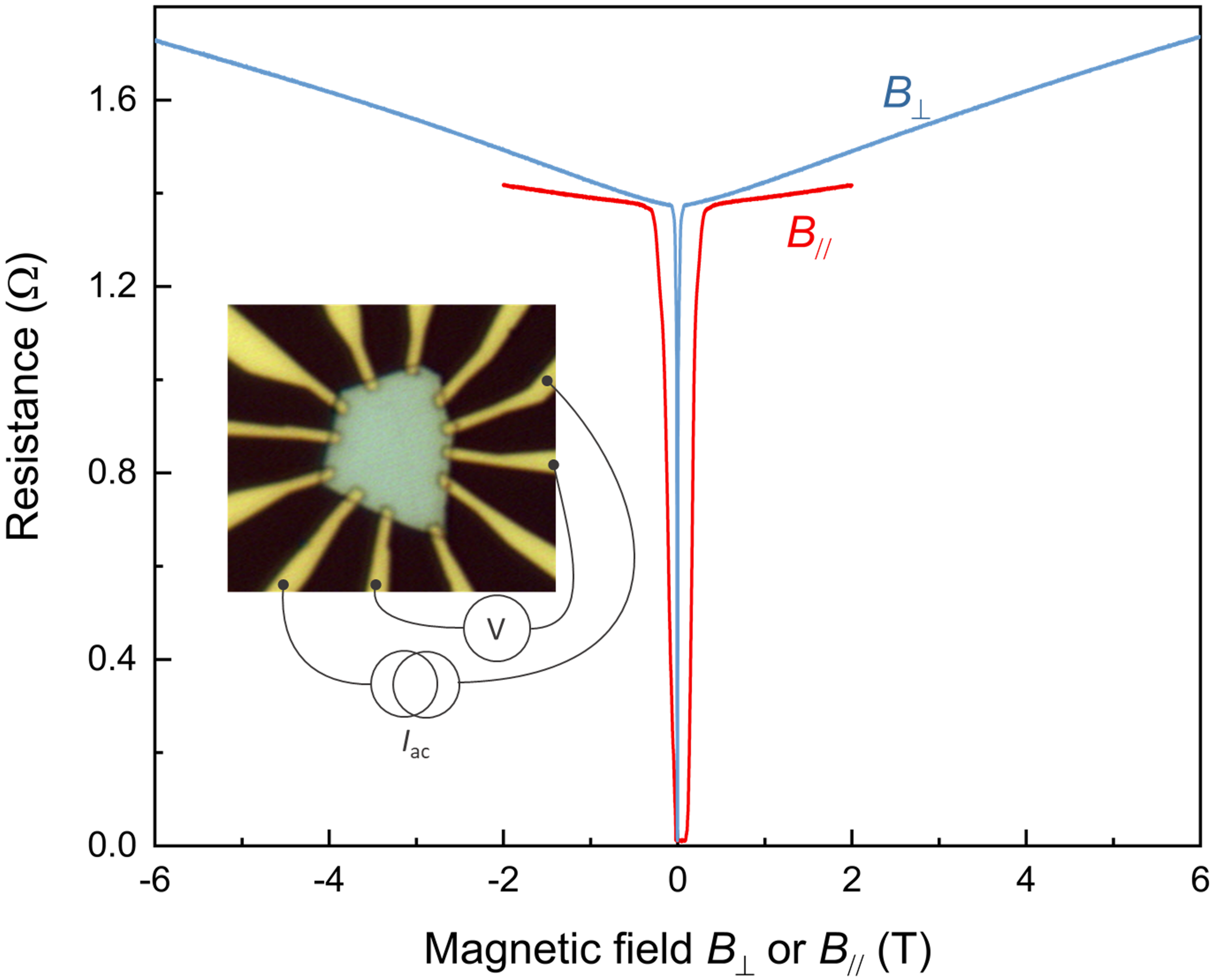

Figure 9: The magnetoresistances at $T \sim 100$ mK for an in-plane and out-of-plane magnetic fields are shown in red and blue respectively. A picture of the sample can be seen in the graph together with the connection configuration for the measurements of the magnetoresistances. The typical size of the sample is about 10 μm.

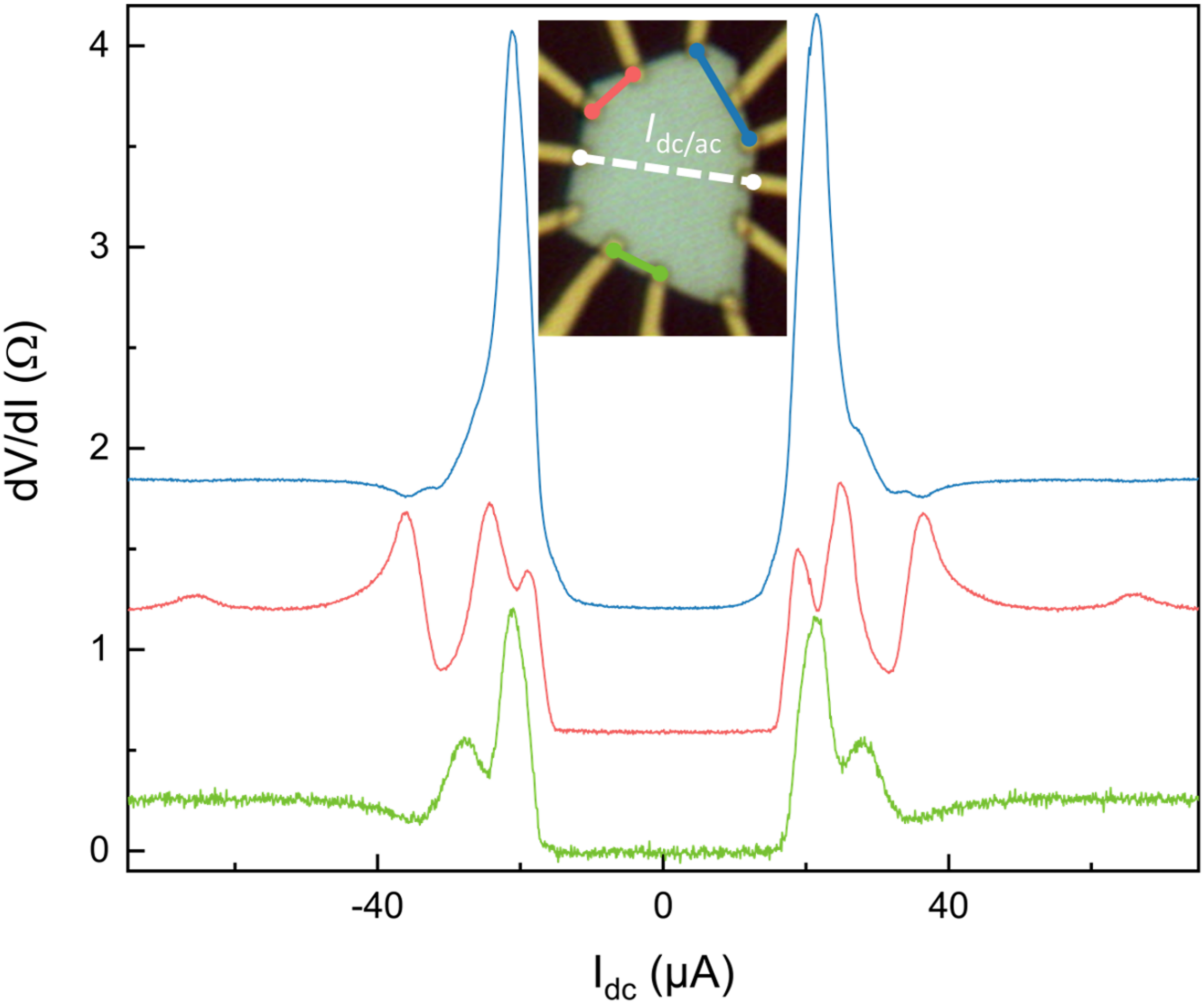

Figure 10: $dV/dI(I_{\rm dc})$ measured at $T \simeq 100$ mK for different set of contacts. The ac current is 1 μA and the differential resistance remains constant for higher dc-current. The contact configuration is indicated in the picture with the colors corresponding to the color of the curves.

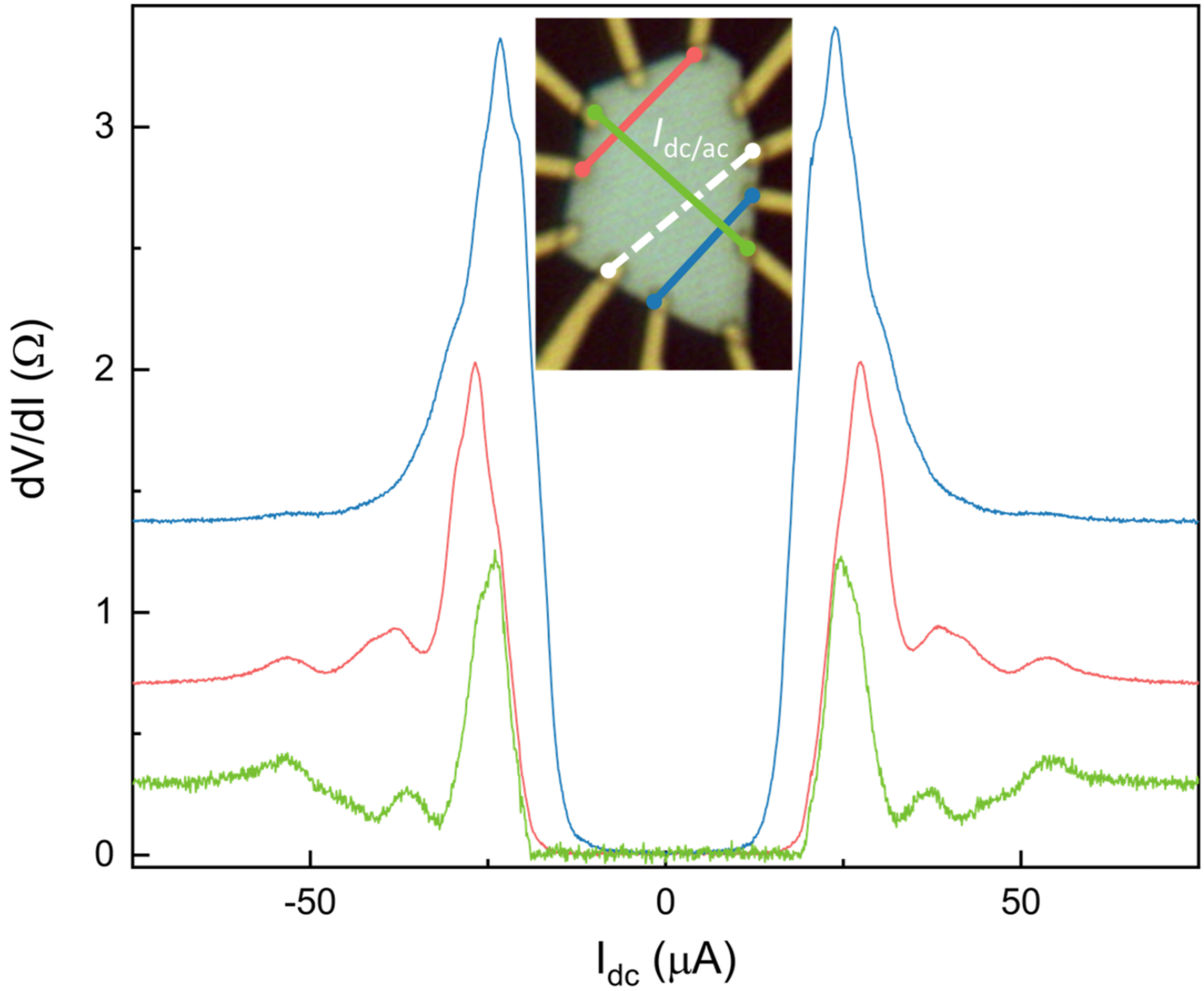

Figure 11: Similar measurements as shown in **??** with different contacts used for both current bias and voltage probes.

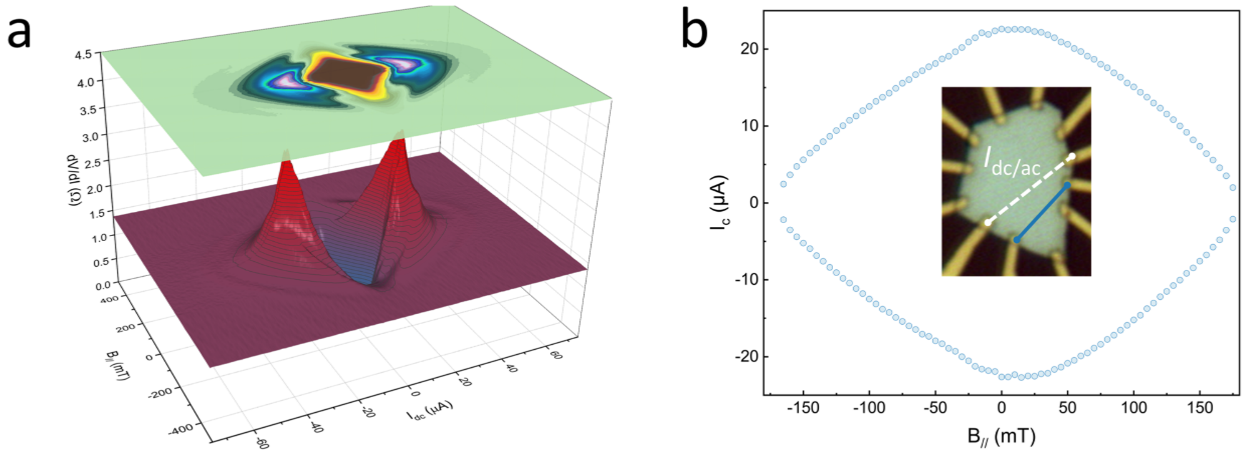

Figure 12: (a) Mapping of $dV/dI(I_{\text{dc}})$ for different parallel magnetic field measured for $-75\mu\text{A} \leq I_{\text{dc}} \leq 75\mu\text{A}$ and with $I_{\text{ac}} = 1\mu\text{A}$. (b) Parallel magnetic field dependency of the critical current as defined in the text for the same contacts as for (a). The contacting configuration is indicated in the inset of (b).

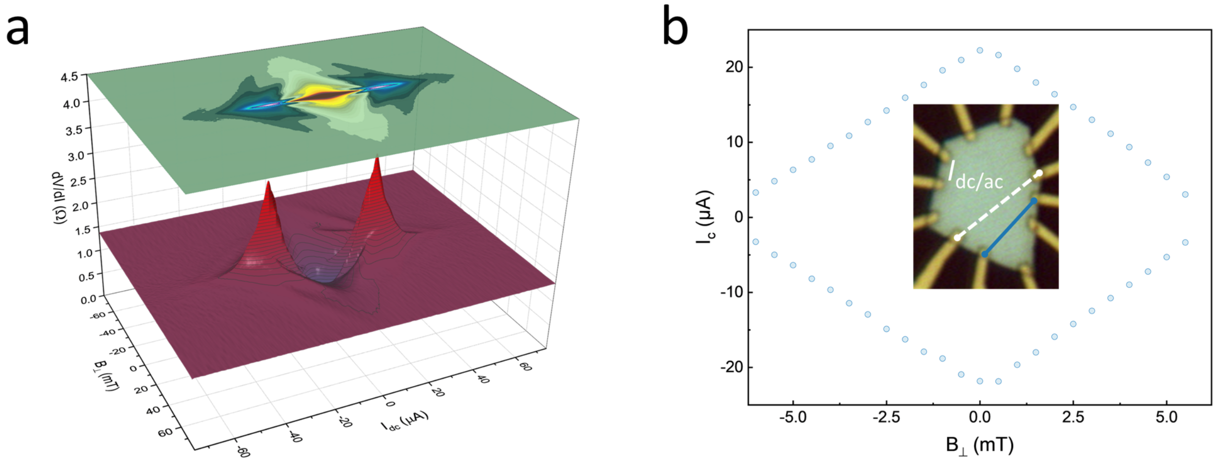

Figure 13: (a) Mapping of $dV/dI(I_{\mathrm{dc}})$ for perpendicular parallel magnetic field measured for $-75\mu\mathrm{A} \leq I_{\mathrm{dc}} \leq 75\mu\mathrm{A}$ and with $I_{\mathrm{ac}} = 1\mu\mathrm{A}$. (b) Perpendicular magnetic field dependency of the critical current as defined in the text for the same contacts as for (a). The contacting configuration is the same as in Figure 12 and is indicated in the inset of (b).

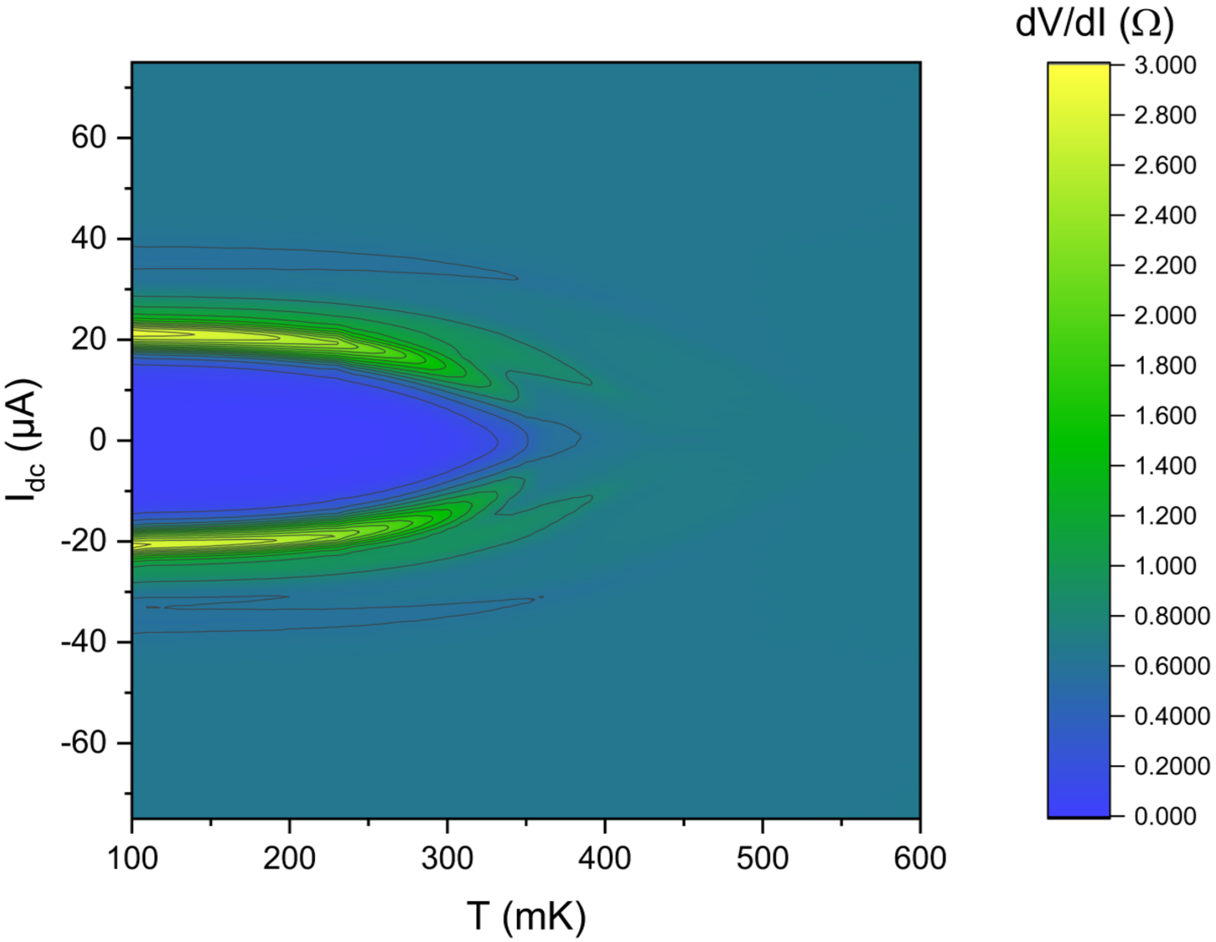

Figure 14: $dV/dI(I_{\mathrm{dc}})$ measured at different temperatures, for $-75\mu\mathrm{A} \leq I_{\mathrm{dc}} \leq 75\mu\mathrm{A}$ and with $I_{\mathrm{ac}} = 1\mu\mathrm{A}$.

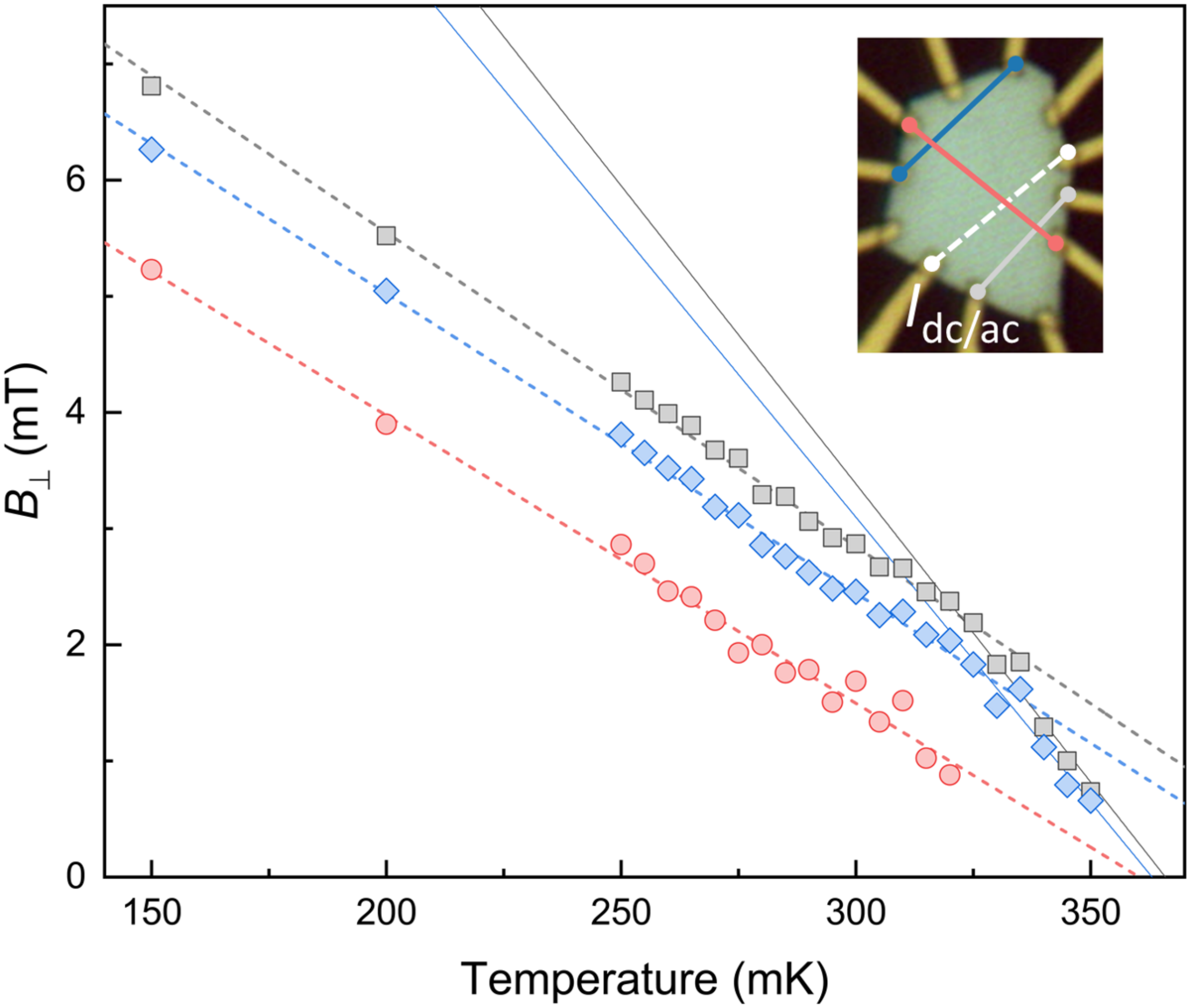

Figure 15: Temperature dependence $B_{\mathrm{c},\perp(T)}$ for different set of contacts indicated in the inset. The blue points are the data points already shown in the main text. The black points are the data points for a set of contact where the discontinuity of the slope is clearly visible, similar to the one reproduced in the main text whereas the red points are the points for which no discontinuity could be measured because of the too low accuracy of the determination of $B_\perp$ close to T_c.

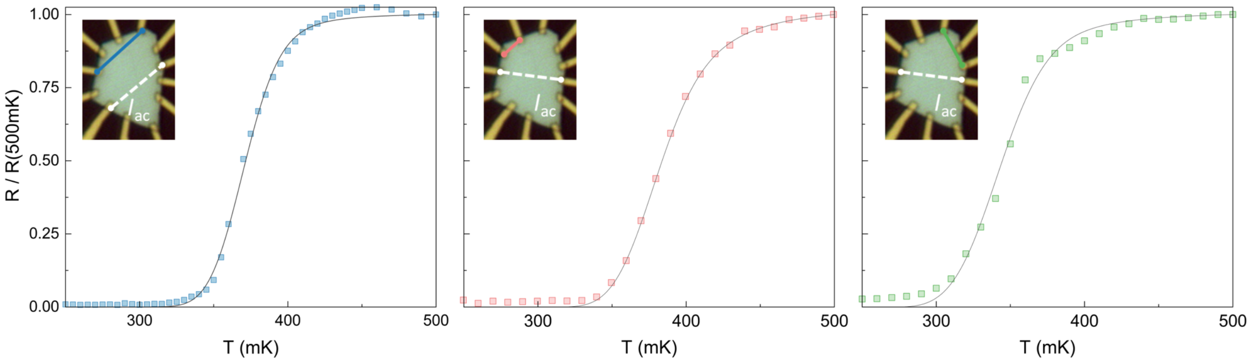

Figure 16: The $R(T)$ measured for different set of contacts indicated in the inset and fitted by Equation (7) in the main text. The ac current was 1 μA and the measurements were done by increasing the temperature by steps of 10 mK with a total stabilization time longer than one hour so that the sample is very well thermalized.